

# Atomistic modeling of epitaxial growth of semiconductor materials



Ignacio Martin-Bragado\*, Andrey Sarikov

IMDEA Materials Institute, Calle Eric Kandel, 2, 28906 Getafe, Madrid, Spain

## ARTICLE INFO

### Article history:

Received 14 July 2015

Received in revised form

12 August 2015

Accepted 17 August 2015

Available online 28 August 2015

### Keywords:

Lattice kinetic Monte Carlo modeling

Solid phase epitaxial regrowth

Metal organic chemical vapor deposition

Defect evolution

Silicon

Gallium arsenide

## ABSTRACT

The epitaxial growth of semiconductors is a very important step for the processing of microelectronic devices. Solid Phase Epitaxial Regrowth (SPER) is involved in both the recrystallization of amorphous silicon and germanium areas. Selective epitaxial growth (SEG) is routinely used in manufacturing modern 3D devices like finFETs, raised source/drain transistors, gate-all-around transistors, etc. In this work, lattice kinetic Monte Carlo modeling is used as the main tool for the modeling and simulation of epitaxial growth in IV and III–V based materials. This is done by detecting particular local configurations at the interfaces, and assigning local growth rates depending on such configurations. This simple idea is used to identify recrystallization planes or to compute different formation energies for the trapping, detrapping and migration of atoms. Introduction of defects is also possible by allowing the formation of twins and small defective areas. We will show different cases where our model is used, namely: SPER and defect formation of Si, and we will explain how the models can be extended to simulate the epitaxial growth of III–V materials and to obtain the different facet formation and growth kinetics. All these cases are compared with relevant experimental results from the literature to provide an assessment of their current capabilities but also possible limitations.

© 2015 Elsevier Ltd. All rights reserved.

## 1. Introduction

Selected parts of contemporary electronic devices such as source/drain regions of integrated circuit transistors, and devices themselves, are fabricated with a trend to miniaturization down to minimum physically achievable dimensions [1]. For the formation of such miniature regions, advanced technologies of structure growth with high spatial resolution, such as selective area epitaxial growth or localized ion implantation with subsequent recrystallization need to be used [1–3]. Growth in small dimensions leads to the manifestation of specific features such as faceting and preferential growth of low index crystalline planes, formation of local strains, evolution of point and extended defects etc. [4–6]. These features have considerable effects both during the structure growth as well as for the device operation. Therefore, they should be taken into account in the modeling of the kinetics of growth processes to reveal underlying physical mechanisms and to enable a reliable control over the behavior of the structures under study both during their formation and normal work regime of devices.

Small size structures favor the application of the modeling methods that enable to obtain the evolution at atomic level, such as *ab initio* [7], molecular dynamics (MD) simulations [8,9], and

lattice kinetic Monte Carlo (LKMC) modeling [10,11]. As compared to the *ab initio* and MD simulations, LKMC methods have a higher scaling potential with preservation of reasonable computation efficiency so that the systems of different sizes can be modeled at low cost. LKMC methods are used to simulate the vast variety of solid transformation kinetics such as e.g. shape relaxation of nanoclusters [12], evolution of the defect structure in solid [13] and laser melted Si [14], vacancy mediated interdiffusion in SiGe alloys [15], step flow growth and defect generation of SiC [16,17], hydrogen adatom [18,19] and vacancy defect [20] evolution in graphene, etc. LKMC modeling can be applied to reveal general peculiarities of a particular process. For example, the change of the relaxation mechanism of the fcc nanocluster shape from the surface atom diffusion to the nucleation of two-dimensional islands on a facet upon reducing the temperature below the roughening threshold has been established without the specification of the cluster material [12]. Alternatively, modeling of the behavior of specific material systems requires proper model calibration with respect to the material properties to obtain reliable results. For such calibration, LKMC methods are often combined with the *ab initio* [18,19] or molecular dynamic [13] simulation methods applied for the smaller scale systems, which provide with the necessary input. In other cases the experimental data sets may be used for the LKMC model calibration. It is also possible that the LKMC results themselves are used for the calibration of macroscopic simulation models such as the kinetics phase field model used to simulate the depth distribution of the vacancy-type

\* Corresponding author. Fax: +34 91 550 30 47.

E-mail addresses: [ignacio.martin@imdea.org](mailto:ignacio.martin@imdea.org) (I. Martin-Bragado), [andrey.sarikov@imdea.org](mailto:andrey.sarikov@imdea.org) (A. Sarikov).

defects arising from the multishot laser irradiation of a Si substrate [14].

In order to improve the modeling power of the LKMC methods, the extended (augmented) lattices are used, in which additional sites are introduced in the standard lattice [15–17]. In [16], the lattice kinetic Monte Carlo model on the “refined” effective lattice including the real lattice sites of the close packed structure as the sub-lattice has been realized. This model has been used to predict the growth regimes and defect formation of the homoepitaxial growth of close packed crystalline structures. In [17], the application of this model to the epitaxial growth of SiC has enabled to describe the peculiarities of the growth rate behavior and defect structure as the functions of the off-cut angle of substrate and the deposition temperature as well as to suggest a new deposition regime, namely “defective epitaxial regime”, between the standard epitaxial step flow and non-epitaxial 2D nucleation regimes. In [15], the LKMC model on the Si lattice augmented with high symmetry sites has been used to simulate the vacancy mediated diffusion in SiGe alloys aimed at the study of the influence of stress and alloy composition on the diffusion mechanism.

This paper presents a brief review of the application of the lattice kinetic Monte Carlo modeling to the study of the kinetics and the peculiarities of the formation of crystalline Si and III–V structures by solid phase epitaxial regrowth (SPER) and metal organic chemical vapor deposition (MOCVD). The algorithms and approaches used to model the defect structures and their evolution during growth, the influence of defects on the growth rate and surface morphology, and the development of preferential faceting are described. In addition, multiscale modeling combining MD, finite-element method (FEM) and LKMC simulations is presented to study the solid phase epitaxial regrowth of amorphized regions in crystalline Si and the formation of their defect structure.

## 2. Lattice kinetic Monte Carlo modeling of solid phase epitaxial regrowth of Si

### 2.1. Anisotropic planar Si regrowth

The kinetics of the solid phase epitaxial regrowth of Si using the lattice kinetic Monte Carlo method is modeled on the ideal Si lattice introduced for the whole system consisting of amorphous and crystalline Si phases with an initially perfect interface between them. The distinction between the Si atoms in both phases is established by assigning the “amorphous” or “crystalline” atoms tags depending on the phase the Si atoms belong. Si atoms have a probability to transfer from the amorphous to the crystalline phase at the amorphous/crystalline interface, which is achieved by changing the respective atom tag. The probability of such transition depends on the orientation of the growing plane of crystalline Si phase, which is a consequence of the geometry of Si atoms incorporation shown schematically in Fig. 1 for {100}, {110} and {111} plane orientations. Following the qualitative model proposed by Drosd and Washburn [21], it is assumed that each atom in the amorphous phase needs to form two undistorted bonds with the crystal to transfer in the crystalline state. This is naturally achieved for {100} oriented surfaces. However, for {110} surfaces a cluster of two adjacent atoms in the amorphous phase is necessary for each Si atom to complete two undistorted bonds, while a cluster of three atoms should form for {111} surfaces, respectively. A coordination number  $n$  is thus associated with each configuration of Si atoms incorporated in the lattice, characterizing the number of simultaneously crystallized Si atoms ( $n=1, 2$  and  $3$  for {100}, {110} and {111} planes orientations, respectively).

The recrystallization kinetics is modeled as a series of consecutive events of a transition of a Si atom from the amorphous in

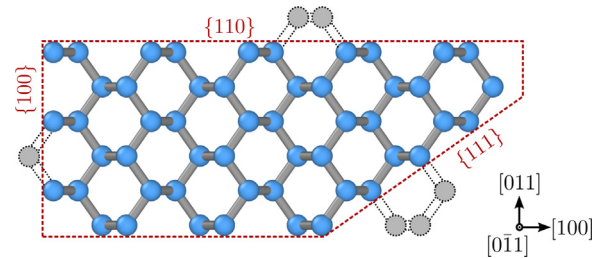


**Fig. 1.** Atomistic configurations for {100}, {011} and {111} local recrystallizations. Si atoms in the crystalline phase are shown inside the contoured geometrical figure, while outside it the sites to be occupied by atoms from the amorphous Si phase are indicated.

the crystalline Si state with the frequency of an event  $f$  calculated as follows [10]:

$$f = K(\text{site}) \times \exp\left(-\frac{E_{\text{activation}}}{kT}\right) \quad (1)$$

using the single activation energy of amorphous-to-crystalline transition  $E_{\text{activation}}$  and three pre-exponential factors characterizing the growth rates of three basic orientations,  $K(100)$ ,  $K(110)$ , and  $K(111)$ , respectively. The values of the parameters in Formula (1) are obtained by model calibration to the available experimental data on the kinetics of the recrystallization of amorphous layers on the top of crystalline Si. Using three pre-exponential factors  $K(100)$ ,  $K(110)$ , and  $K(111)$ , the different recrystallization rates for the three mentioned basic plane orientations are obtained as well as the formation of faceted structures during recrystallization (see Fig. 2) [10], in agreement with the results of experimental observations [22]. In addition, the effect of the strain appearing as a result of  $\sim 2\%$  volume mismatch between amorphous and crystalline Si [23] and leading to the retardation of recrystallization is successfully accounted for by modifying the value of  $E_{\text{activation}}$  with strain related components as further described in Section 2.3.

The LKMC model described in this section is further modified to include the formation of the twin defects during amorphous Si epitaxial regrowth [24]. These defects are known to influence on the SPER rate and structure, including the shape and the interface roughness between the amorphous and crystalline Si phases. To model the formation of twin defects during the SPER process, the Si atoms in the lattice sites after the recrystallization event are assigned one of the following two tags, namely: *normal* for the sites sharing the substrate configurations, and *defective* for the sites that are assumed not to bond properly to their neighbors but to form twin defects similar to those observed in MD simulations [9,25]. New defective sites are produced by either of the two mechanisms: (i) {111} sites (and thus related with the  $K(111)$  pre-exponential factor) have a probability  $P_{\text{def}}^{(111)}$  of becoming defective,

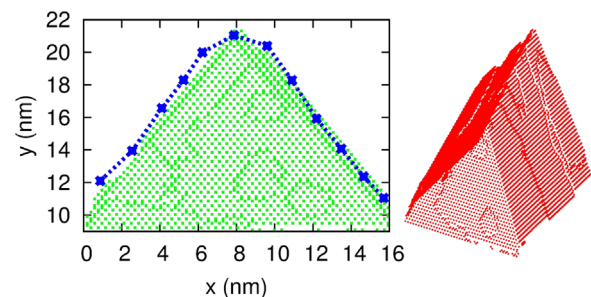


**Fig. 2.** Left: arrow tip formation during SPER of a thin Si fin ( $16 \times 50 \text{ nm}^2$ ). Simulation results (symbols) and experimental amorphous/crystalline regrowth (line, taken from [22]) after a 60 s, 600 °C annealing are presented. Right: 3D view of the same simulation.

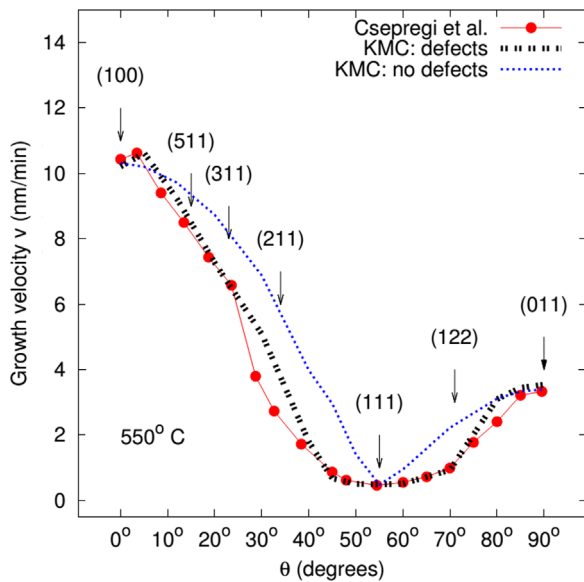


**Fig. 3.** Comparison of experimental SPER velocities (symbols) taken from Csepregi et al. [26] to different LKMC simulations when the creation of defects during the process is (thick dashed line) or is not (thin dashed line) modeled. The angle is specified with respect to the orientation away from {100} and towards {011}. The model correctly reproduces the dependence of SPER velocity at 550 °C on the substrate angle.

and (ii) Si atoms recrystallize in the proximity of defective sites through local {111} or {011}, but not {100}, recrystallizations, inheriting respective tags and becoming defective themselves. The definition of the coordination number  $n$  used to recognize the different sites of the incorporation of Si atoms in the crystalline Si lattice is extended in the model to distinguish between recrystallized defective and normal atoms too. Consequently, the creation of defective sites affects subsequent epitaxial regrowth by lowering  $n$ , thus changing the local SPER kinetics and serving as a seed to create more twin defects.

The comparison of the experimental data on the regrowth rate at 550 °C on the misorientation angle of crystalline Si with respect to {100} orientation in the direction of {110} plane [26], with the modeled SPER velocities with (thick dashed line) and without (thin dashed line) defect formation is shown in Fig. 3. It can be seen from this figure that excellent agreement with the experimental results is achieved when defect generation is permitted. The data in Fig. 3 confirm the importance of the account of twin defect formation during modeling the SPER process. The creation of defects causes the rate of SPER to slow down. In balancing the recrystallization rate and twin defect formation during the SPER process,  $K(111)$  should be considered as the most important parameter. High values of  $K(111)$  introduce high amounts of defects thus significantly affecting the growth rate for all crystalline Si orientations. On the other hand, the decrease in the  $K(111)$  value mainly influences the growth of Si{111} orientation and forces the system to recrystallize through {100} and {110} local events for all other orientations. Proper calibration of  $K(111)$  to ensure the agreement between the experimental and modeled dependence of the Si growth rate, as shown in Fig. 3, demonstrates that the recrystallization is partially or completely degenerated into {111} recrystallization and defect formation in the range of the misorientation angles of 40° to 70°. This leads to the formation of highly defective Si layers after recrystallization for mentioned orientations, in good agreement with experimental observations [22].

## 2.2. Epitaxy on Si(111) substrates

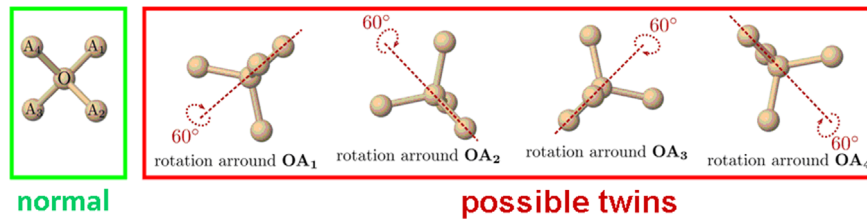
A special case of the solid phase epitaxial regrowth of amorphous Si is represented by the SPER on the Si(111) substrates, which takes place with two different velocities, depending on the thickness grown, and with the change of the surface roughness correlating with the velocity change [27,28]. Such complexity is produced by the formation of twins that determine the kinetic of the recrystallization at later (faster) stages [29]. To tackle this complexity, a comprehensive physical LKMC model is implemented that incorporates defect formation, to explain micro-twin formation, bi-modal Si(111) growth, and interfacial topology. It differs from the model presented in the previous section by that four, instead of three, local configurations of Si atoms incorporation, namely {100<sub>l</sub>}, {100<sub>h</sub>}, {110}, and {111} are considered. The definition of two configurations for {100} helps to better control the amorphous/crystalline interface, and takes into account the number of second neighbors to distinguish between low {100<sub>l</sub>} and high {100<sub>h</sub>} coordinations [11]. In addition, unlike setting the *normal* or *defective* tags to the crystallized Si atoms, the model takes into account the actual geometry of twin formation during filling new lattice atoms.

Fig. 4 contains all the valid configurations representing the substrate lattice and its twin configurations used by the simulator. The geometries of the twin formation set additional sites to the Si lattice that can be occupied with Si atoms, similar to the augmented lattice sites described in [16]. A twin is seen as a 60° rotation with respect to one bond in the original Si-Si<sub>4</sub> tetrahedron of the Si lattice. After the initial substrate is provided, the model used here detects the local orientations using first and second neighbor distances and grows the crystal by picking the right match in the configuration table. For {100} and {110} local configurations surrounded by perfect crystal, there is only one match. But for {111} local configurations there are actually two matches: the current orientation and the twin orientation. In both of them the bond to the crystal is the same, but the rest of the tetrahedron is not specified and admits the rotation of 60° contained in the twin configuration. Under these circumstances, one of the two configurations is randomly picked. If the twin is chosen, subsequent recrystallization of neighboring atoms detects it and attaches to the amorphous/crystalline interface with such orientation, extending it. Finally, when regular and twin crystallized parts meet, none of the two configurations is to be detected: atoms in such conditions are defects. Consequently a twin region is not defective *per se*, only the stacking faults are created at the intersection of different regions.

Fig. 5 shows the comparison of simulated thicknesses of recrystallized Si layers (symbols) with experimental ones (solid lines) at 550 °C [27]. The dashed line shows the averaged values for several Si(111) simulations performed with different starting random seeds, which results are also shown as red symbols. There is a perfect agreement for Si{100}, Si{110}, and the first nanometers of Si{111}. For Si{111} growth above 100 nm, the referred experimental work [27] shows a sudden change into a faster recrystallization speed, which is also seen in the simulations. At this, the partial disagreement between experimental data and simulations for this fast recrystallization velocity for Si{111} is called by a relatively small simulation domain not allowing to collect enough statistics, as explained in more detail in our previous publication [28].

The simulated Si structures representing the roughness evolution of recrystallized Si(111) layers are shown in Fig. 6(c) and (d). For comparison, the modeling result for Si with {100} and {110} orientations is also demonstrated revealing rather flat amorphous/crystalline interfaces (Fig. 6(a) and (b)). Our simulations for Si{111}, made at 550 °C, correlate both the change of the recrystallization





**Fig. 4.** Formation of twin configurations during SPER of Si with (111) orientation. The left part shows the Si-Si<sub>4</sub> tetrahedron of the Si lattice in its normal orientation. The twins are formed by the 60° rotation around one bond of the tetrahedron as displayed in the right part of the figure.

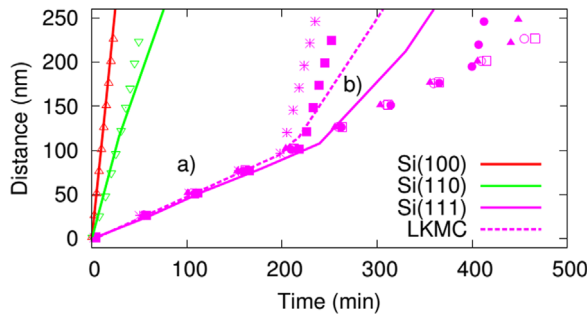


**Fig. 5.** Experimental data [27] (solid lines) versus simulated results (symbols) for Si (100), Si(110), and Si(111) regrown distance with time. Results with different random seeds, together with their average (dashed line), are shown for Si(111). Our model can produce and explain the two different velocities (a) and (b) experimentally seen in Si(111) SPER. (For interpretation of the references to color in this figure, the reader is referred to the web version of this article.)

velocity and the formation of surface non-uniformity, explaining them in terms of the creation of twins that do not grow parallel to the (111) substrate orientation. Initially, a very slow local Si(111) recrystallization takes place leading to the formation of both regular and twin islands grown epitaxially on (111) substrates. At this stage the amorphous/crystalline interface is mostly flat (see Fig. 6 (c)) and the growth rate corresponds to the part (a) in Fig. 5. The growth progress of two existing crystallographic orientations of islands results in the formation of stacking faults parallel to the interface, at their intersection. These stacking faults are a source of other {111} facets to grow laterally and to form twins that will have a different orientation than the previous ones. The geometrical structure of such defect is shown in Fig. 7. Formation of inclined structures changes the mechanism of the recrystallization of amorphous Si to the mixed <110> mechanism in the direction, different from the perpendicular to initial substrate and with the different (higher) velocity. In its turn, this leads to the increase of the surface roughness as demonstrated by Fig. 6(d).

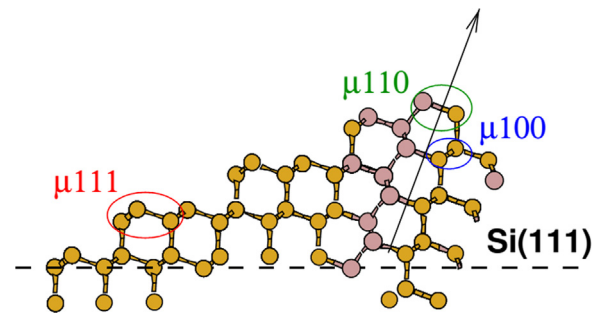


**Fig. 7.** Inclined twin structure in the Si(111) epitaxial regrowth. The arrow points on the growth direction according to the mixed <110> mechanism. Difference in the growth rates of {100}, {110}, and {111} orientations (marked here as  $\mu_{100}$ ,  $\mu_{110}$ , and  $\mu_{111}$ , respectively) leads to the development of high surface roughness after the formation of inclined twin structure.

### 2.3. Multiscale modeling of solid phase epitaxial regrowth

Multiscale modeling of SPER process is used to give further insight into the defect formation mechanisms, and to shed light on their effect on the regrowth and their relation with the internal strains generated by the amorphous/crystalline volume mismatch [30]. Here, three different techniques have been used, namely finite element method (FEM), molecular dynamics (MD) and lattice kinetic Monte Carlo (LKMC). FEM calculations provide the strain pattern generated by the volume expansion of the amorphous Si phase as well as its dependence on the dimensions of amorphous Si system. This strain affects the recrystallization rate and the generation of defects during this process, as revealed by MD simulations.

MD simulations demonstrate that in the strain free case (corresponding to the small dimensions of amorphous Si system) the formation of twins during regrowth as a result of the development of {111} planes is observed. Appearance of strain (larger amorphous Si dimensions) leads to the slowing down the

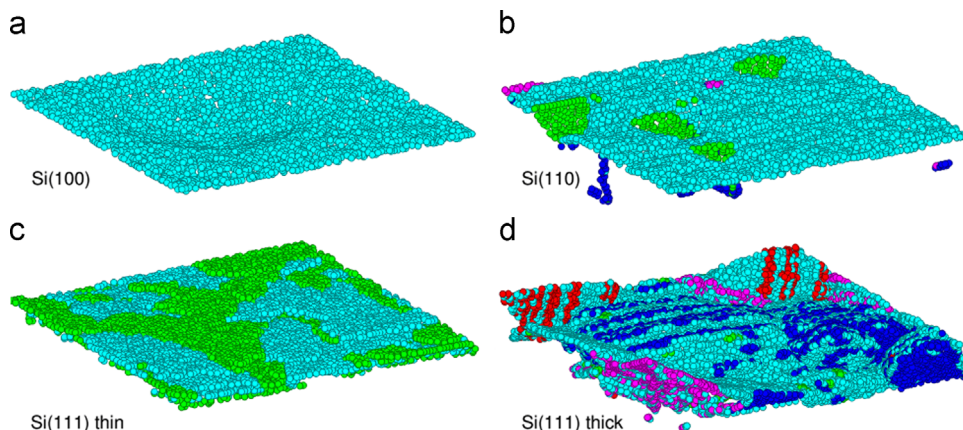


**Fig. 6.** Simulated amorphous/crystalline interface topology for Si substrates with (100), (110), and (111) orientations grown at 550 °C. Thin samples of Si(111) are quite uniform, while thick samples of Si(111) have increasing roughness, in agreement with experimental observations [27].

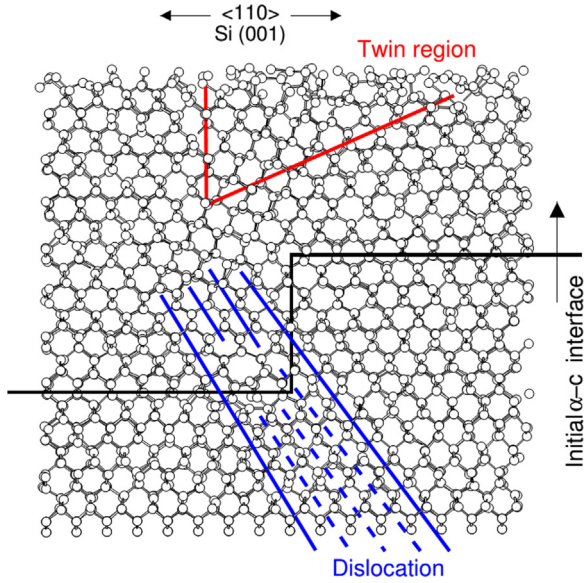


**Fig. 8.** Cross sectional image of the complete regrowth of  $\langle 110 \rangle$ -aligned amorphous Si region in Si(001) under compressive external stress. The regions of the formation of two types of defects, namely microtwins and dislocations, are indicated.

recrystallization and the formation of  $\{111\}$  facets, which, after collapsing, leave a pattern of mask-edge defects. Fig. 8 shows the MD simulated image of a completely recrystallized amorphous Si regions with  $\langle 110 \rangle$  alignment on Si(001) substrate [30]. As one may see from this figure, two non-equivalent defects are formed during such recrystallization, namely microtwins, which are developed due to the stability of  $\{111\}$  planes, and dislocations, which are formed when two fronts, originally from the same substrate, produced by the slow-down of shear strain, collapse.

The LKMC method, integrated with FEM for the mechanical calculations, has been used to simulate the evolution of SPER for realistic sample sizes and annealing temperatures. As the MD simulations previously shown indicate three important physical mechanisms, namely: (i) the formation of twins, (ii) the slowed down recrystallization near the corners as a consequence of the shear strain, and (iii) the collapse of the two recrystallization fronts induced by (ii) and further formation of dislocations, they all need to be scaled up into LKMC. The formation of twins is included as described in previous section [28] and the strain is treated by coupling the LKMC model to the FEM module mentioned above.

The simulation procedure looks as follows. Iteratively, the LKMC transforms amorphous Si into crystalline. The structure is accounted for by the FEM module, which computes the strains associated with the volume expansion of amorphous Si and transfers the strains back to modify the regrowth rates. Finally, the collapse of the two fronts is a natural cause of the previous steps and does not need to be explicitly modeled. The activation energy of LKMC simulations (see Expression (1)) undergoes correction, which proceeds in two steps. First, the non-shear corrections are introduced as explained in [31], after which an extra slow-down produced by the shear strain  $\epsilon_{xy}$ , in agreement with the experimental observations of [32], is accounted for as

$$E = E_{\text{activation}} + \epsilon_{xy}^2 K \quad (2)$$

where  $K = 9 \times 10^3$  eV is the parameter that has been fitted to properly reproduce experimental observations.

Fig. 9 presents several snapshots at different stages of the SPER process for (001) orientations of the Si substrate aligned in the  $\langle 110 \rangle$  direction. For clarity, only the atoms at the amorphous/crystalline interfaces are represented.

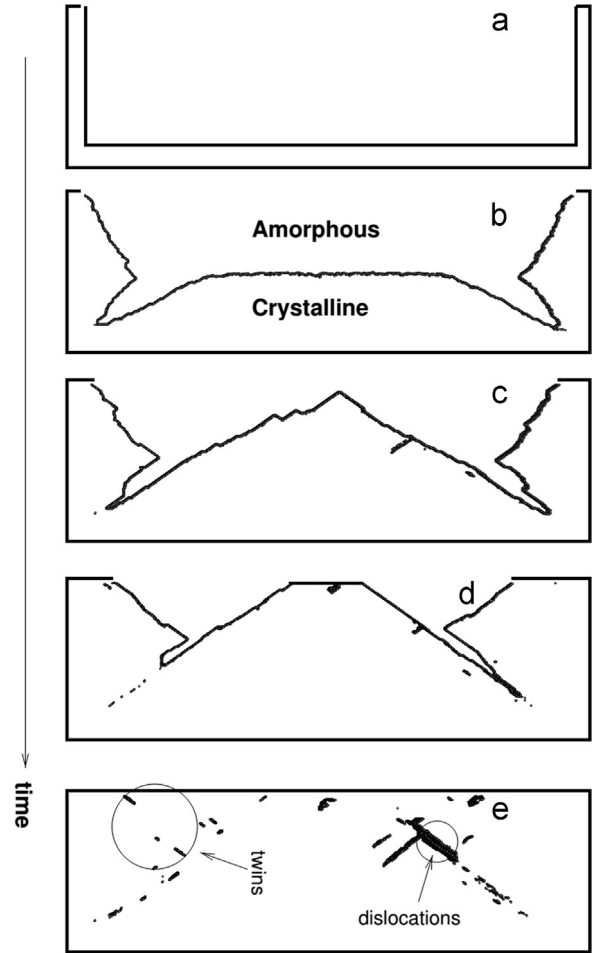


**Fig. 9.** LKMC simulation snapshots of the recrystallization of  $\langle 110 \rangle / \langle 001 \rangle$  Si substrate at different stages of the annealing at 550 °C. Defected regrowth regions and defect types are indicated in bottom view. While LKMC cannot determine the defect categories, the MD studies allow us to identify their types, as indicated in the figure.

As demonstrated by Fig. 9(b), the formation of  $\{111\}$  facets takes place, which act as a template for the progressive recrystallization. The regrowth at the corners is seen to be slowed down. With the progress of recrystallization, the formation of downturned edges occurs, which evolve into edge triangular pockets, as shown in Fig. 9(e). These pockets remain after complete regrowth has been achieved. Obtained results are in noticeable agreement with the experimentally observed evolution of similar topologies observed in [33,34]. The extended defects predicted by LKMC are also validated by the results of the cross-sectional transmission microscopy observations reported by Saenger et al. [35]. In general, the combined use of different simulation methods with the transfer of information between them is demonstrated to provide a reliable technique for simulating realistic experiments.

### 3. MOCVD epitaxial growth of III–V semiconductors

In this section, the aspects of LKMC modeling are considered to study the kinetics and morphology of the homoepitaxial growth of III–V materials, in particular GaAs. To grow the GaAs structures epitaxially from the gas phase, metal organic chemical vapor deposition with trimethylgallium (TMG) and arsine ( $\text{AsH}_3$ ) precursors is widely used [36]. Numerical modeling of the kinetics and mechanisms of the process under study was considered in

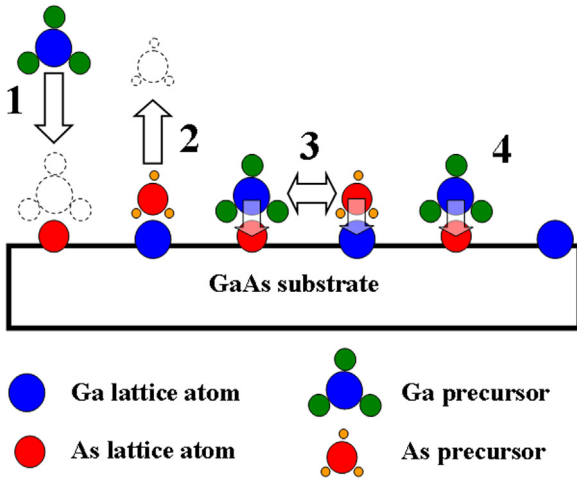


Fig. 10. Elementary processes during the MOCVD epitaxial growth of GaAs layers.

many previous publications, including our recent work [37]. Such approach enables to obtain the average values of the parameters characterizing the growth mechanisms. Comparing to the numerical modeling, lattice kinetic Monte Carlo represents a more powerful technique that makes possible an investigation of the peculiarities of epitaxial process at atomic scale and disclose the growth mechanisms as functions of local atomic configurations.

The mechanisms, which are in action during the GaAs epitaxy, are shown schematically in Fig. 10 [37]. They include: (i) adsorption/desorption of precursor molecules on the specific surface sites associated with As and Ga surface atoms (for TMG and AsH<sub>3</sub> adsorption, respectively) (processes 1 and 2), (ii) pairwise interaction of adsorbed precursors to produce free Ga and As atoms, which build up the lattice (process 3), and (iii) decomposition of single precursor molecule with extraction of either Ga or As atom alone (process 4). Each process is characterized by a frequency calculated analogous to Expression (1), apart from the adsorption frequency, which is determined according to the molecular kinetic theory of ideal gases. The parameters for kinetic Monte Carlo modeling are fitted with respect to the experimental results on the dependence of the growth rate on the temperature and orientation of GaAs layers presented in [36]. In Fig. 11, the dependences of the thickness of GaAs (110) layers on time calculated for different temperatures by Monte Carlo algorithm are compared with the analogous results obtained by numerical simulations [37] revealing their perfect consistency.

More complex LKMC model uses the algorithm proposed by

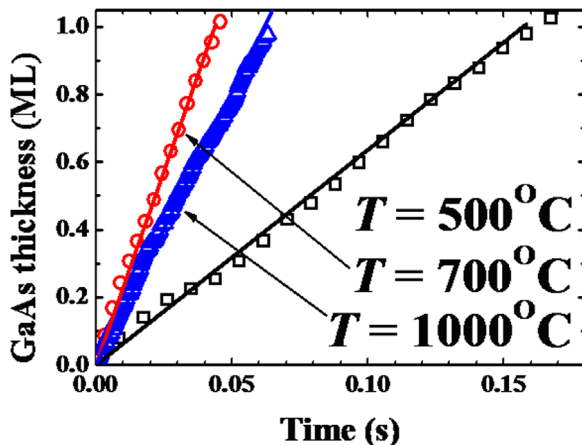


Fig. 11. Dependence of the thickness of GaAs layer on time for three deposition temperatures calculated by Monte Carlo (symbols) and numerical (lines) modeling.

Chen and Choi [38], in which the activation energy of the atom incorporation in the lattice (Ga and As atoms for our case, see processes 3 and 4 in Fig. 10) depends on the binding interactions with the nearest neighbors to the incorporation site up to third coordination sphere. The frequency of atom incorporation in the lattice is described by the following expression:

$$f_{\text{incorporation}} = K_0 \times \exp\left(-\frac{E_0 - |E_b|}{kT}\right) \quad (3)$$

where  $E_0$  is some basic energy value and the energy characterizing the binding interaction with nearest neighbors is calculated as

$$E_b = E_b^{1NN}(n_1) + n_2 E_b^{2NN} + n_3 E_b^{3NN} \quad (4)$$

In the Expression (4),  $n_i$  is the number of  $i$ -th nearest neighbors and  $E_b^{iNN}$  is the respective energy characterizing the binding interaction with the atom being incorporated in the lattice. The contributions to  $E_b$  for the second and third neighbors are calculated as proportional to the values of  $n_2$  and  $n_3$ , while for the first neighbors non-scalable  $E_b^{1NN}(n_1)$  corresponds to each value of  $n_1$  [38].

In contrast to the models described in Section 2, use of the incorporation frequency (3) enables to take into account different growth rates of different plane orientations in a natural way with a single pre-exponential parameter  $K_0$  and a single set of energy values  $E_0$  and  $E_b^{iNN}$ . As an example, Fig. 12 shows the simulated

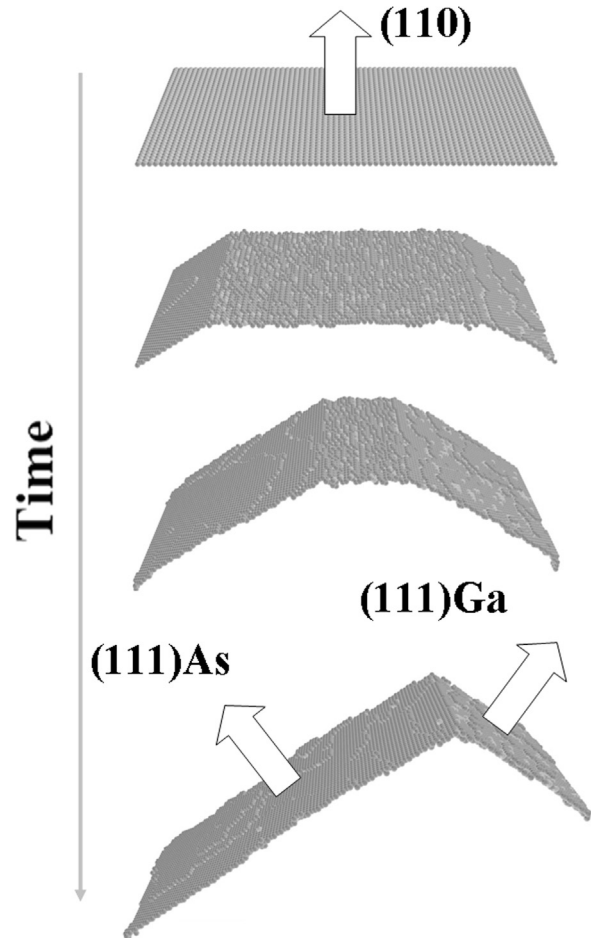


Fig. 12. Development of the {111} facets of initially flat {110} GaAs plane with the time of MOCVD epitaxial growth. The area of Ga terminated {111} plane grows faster than As terminated plane due to higher partial pressure and lower desorption of As containing precursors. As terminated surfaces (dark gray atoms) develop during growth despite equal quantities of both Ga (light gray atoms) and As atoms are present initially on the GaAs {110} surface.



evolution of the initially (110) oriented GaAs surface with the deposition time. The technological parameters of the deposition corresponded to the experiments described in [36]. Although proper calibration of the model to perfectly fit the experimental data is still lacking, the results in Fig. 12 reproduce the experimentally observed features, such as (i) slower growth rate of {111} planes relative to {110} planes, which leads to the turnover of the GaAs interface from the horizontal (110) plane to the {111} faceted structure with the deposition progress, (ii) faster growth of Ga terminated {111} plane as compared to As terminated one, manifested by the smaller area of the former, and (iii) As termination of GaAs surfaces despite equal initial surface concentrations of Ga and As atoms on the GaAs (110) plane. The latter two effects are called by about an order of magnitude higher partial pressure of As containing precursor in the gas phase as well as its lower desorption rate as compared to Ga containing precursor, as found by numerical simulations [37]. Further development of the model described, in application to the epitaxial growth of GaAs and other III–V semiconductors, to be fulfilled in future investigations, will provide the efficient tool for the simulation of the growth kinetics of structures with different geometries, as demanded by contemporary microelectronics, as well as for the understanding the physical mechanisms associated with the growth peculiarities.

#### 4. Conclusions

In this work, the approaches to study the kinetics of the solid phase epitaxial regrowth of Si and MOCVD growth of III–V semiconductor structures using lattice kinetic Monte Carlo methods are reviewed. Application of LKMC methods with proper calibration enables to disclose the mechanisms associated with the mentioned processes such as the formation and evolution of defects and appearance of preferential facets during growth, as well as the influence of defects and strain on the growth rate and layer morphology. Moreover, LKMC methods are efficient to apply as a part of the multiscale modeling algorithms, in which the advantages of several modeling methods are exploited with information exchange, enabling to characterize the processes under study more completely and with less usage of fitting procedures.

#### Acknowledgment

The authors want to acknowledge B. Sklenard and M. Prieto-Depedro for contributions to the preparation of some figures. This work has been carried in the framework of the European Union research project COMPOSE<sup>3</sup> (ICT-2013-11-619325). The

contribution of I. Martin-Bragado was supported by the Ramón y Cajal Fellowship (RyC-2012-10639). A. Sarikov acknowledges the support of his work by the AMAROUT II Fellowship PCOFUND-64-2011-291803.

#### References

- [1] G.L. Olson, J.A. Roth, *Mater. Sci. Rep.* 3 (1988) 1–77.
- [2] E. Gil-Lafon, J. Napierala, D. Castellucci, A. Pimpinelli, R. Cadoret, B. Gérard, *J. Cryst. Growth* 222 (2001) 482–496.
- [3] T. Aoyama, T. Ikarashi, K. Miyana, T. Tatsumi, *J. Cryst. Growth* 136 (1994) 349–354.
- [4] S.C. Lee, D.L. Huffaker, S.R.J. Brueck, *Appl. Phys. Lett.* 92 (2008) 023103.
- [5] N. Rudawski, K. Jones, *Scr. Mater.* 61 (2009) 327–330.
- [6] N. Burbure, N. Rudawski, K. Jones, *Electrochem. Solid State Lett.* 10 (2007) H184–H185.
- [7] F. Gao, E.J. Bylaska, W.J. Weber, L.R. Corrales, *Phys. Rev. B* 64 (2001) 245208.
- [8] B.A. Gillespie, H.N.G. Wadley, *J. Cryst. Growth* 311 (2009) 3195–3203.
- [9] E. Lampin, C. Krzeminski, *J. Appl. Phys.* 106 (2009) 063519.
- [10] I. Martin-Bragado, V. Moroz, *Appl. Phys. Lett.* 95 (2009) 123123.
- [11] I. Martin-Bragado, V. Moroz, *Appl. Phys. Lett.* 98 (2011) 153111.
- [12] N. Combe, P. Jensen, A. Pimpinelli, *Phys. Rev. Lett.* 85 (2000) 110–113.
- [13] A. La Magna, S. Coffa, L. Colombo, *Phys. Rev. Lett.* 82 (1999) 1720–1723.
- [14] A. La Magna, V. Privitera, G. Fortunato, M. Cuscunà, B.G. Svensson, E. Monakhov, K. Kuitunen, J. Slotte, F. Tuomisto, *Phys. Rev. B* 75 (2007) 235201.
- [15] R. Chen, S.T. Dunham, *J. Vacuum Sci. Technol. B* 28 (2010), C1G28–C1G23.
- [16] M. Camarda, A. La Magna, F. La Via, *J. Comput. Phys.* 227 (2007) 1075–1093.
- [17] F. La Via, M. Camarda, A. La Magna, *Appl. Phys. Rev.* 1 (2014) 031301.
- [18] I. Deretzis, A. La Magna, *Nanoscale* 5 (2013) 671–680.
- [19] F. Gargiulo, G. Autès, N. Virk, S. Barthel, M. Rösner, L.R.M. Toller, T.O. Wehling, O.V. Yazyev, *Phys. Rev. Lett.* 113 (2014) 246601.
- [20] T. Trevethan, C.D. Latham, M.I. Heggie, P.R. Briddon, M.J. Rayson, *Nanoscale* 6 (2014) 2978–2986.
- [21] R. Drosd, J. Washburn, *J. Appl. Phys.* 53 (1982) 397–403.
- [22] R. Duffy, M.V. Dal, B.J. Pawlak, M. Kaiser, R.G.R. Weemaes, B. Degroote, E. Kunnen, E. Altamirano, *Appl. Phys. Lett.* 90 (2007) 241912.
- [23] J. Custer, M. Thompson, D. Jacobson, J. Poate, S. Roorda, W. Sinke, F. Spaepen, *Appl. Phys. Lett.* 64 (1994) 437–439.
- [24] I. Martin-Bragado, *Scr. Mater.* 66 (2012) 186–189.
- [25] C. Krzeminski, E. Lampin, *Eur. Phys. J. B* 81 (2011) 283–290.
- [26] L. Csepregi, E.F. Kennedy, J.W. Mayer, T.W. Sigmon, *J. Appl. Phys.* 49 (1978) 3906–3911.
- [27] L. Csepregi, J.W. Mayer, T.W. Sigmon, *J. Appl. Phys.* 29 (1976) 92–93.
- [28] I. Martin-Bragado, B. Sklenard, *J. Appl. Phys.* 112 (2012) 024327.
- [29] M.D. Rehtin, P.P. Pronko, G. Foti, L. Csepregi, E.F. Kennedy, J.W. Mayer, *Philos. Mag. A* 37 (1978) 605–620.
- [30] M. Prieto-Depedro, I. Romero, I. Martin-Bragado, *Acta Mater.* 82 (2015) 115–122.
- [31] B. Sklenard, J.-C. Barbe, P. Batude, P. Rivallin, C. Tavernier, S. Cristoloveanu, I. Martin-Bragado, *Appl. Phys. Lett.* 102 (2013) 151907.
- [32] Y. Shin, J. Lee, M. Park, H.J. Kang, *J. Cryst. Growth* 231 (2001) 107–114.
- [33] S. Morarka, N. Rudawski, M. Law, *J. Vacuum Sci. Technol. B* 26 (2008) 357–361.
- [34] H. Cerva, K. Küsters, *J. Appl. Phys.* 66 (1989) 4723–4728.
- [35] K. Saenger, K. Fogel, J. Ott, D. Sadana, H. Yin, *J. Appl. Phys.* 101 (2007) 104908.
- [36] D.H. Reep, S.K. Ghandi, *J. Electrochem. Soc.* 130 (1983) 675–680.
- [37] A. Sarikov, I. Martin-Bragado (submitted for publication).
- [38] R. Chen, W. Choi, in: *Proceedings of the 18th International Conference on Simulation of Semiconductor Processes and Devices SISPAD 2013*, Glasgow, UK, 28–30 August 2013, pp. 9–12, tp.